Hydrous hydrazine decomposition over Rh/Al2O3 catalyst: Experimental and CFD studies

Hydrous Hydrazine decomposition over Rh/Al_2O_3 catalyst: Experimental and CFD Studies

Panayiota Adamou[1], Silvio Bellomi[2], Eleana Harkou[1], Xiaowei Chen[3], Juan J. Delgado[3], Nikolaos Dimitratos[4,5], George Manos[6], Alberto Villa*[2], Achilleas Constantinou[1]*

[1] Department of Chemical Engineering Cyprus University of Technology, 57 Corner of Athinon and Anexartisias, 3036 Limassol, Cyprus.

[2] Dipartimento di Chimica, Universitá degli Studi di Milano, via Golgi, 20133 Milan, Italy.

[3]Departamento de Ciencia de los Materiales, Ingeniería Metalúrgica y Química Inorgánica, Facultad de Ciencias, Universidad de Cádiz, Campus Río San Pedro, Puerto Real (Cádiz) E-11510, Spain

[4]Department of Industrial Chemistry "Toso Montanari", Alma Mater Studiorum University of Bologna, Viale Risorgimento 4, 40136 Bologna, Italy.

[5] Center for Chemical Catalysis-C3, Alma Mater Studiorum University of Bologna, Viale Risorgimento 4, 40136 Bologna, Italy.

[6] Department of Chemical Engineering, University College London, London WCIE 7JE, UK.

* Authors for correspondence: a.konstantinou@cut.ac.cy; alberto.villa@unimi.it

Abstract

Addressing challenges associated with fossil fuels emissions and contributing to a sustainable energy future is the main objective of the science community. Hydrogen (H_2) is emerging as a promising future fuel promoting clean energy production. In this work, the catalytic decomposition of hydrous hydrazine was evaluated using a commercial 0.5 wt.% Rh/Al_2O_3 catalyst for H_2 generation. The reaction conditions for the catalyst were optimised in a batch reactor, and computational fluid dynamics (CFD) simulations were performed, accurately validating the results. CFD studies were also conducted on velocity and temperature magnitude and, reactant concentration and catalytic particles distribution in the reactor area, highlighting the key role of the systems' uniformity on maximum H_2 generation. This work is the first, to our knowledge, which uses computational simulation on hydrous hydrazine decomposition, contributing to better understand the reaction kinetics, providing insights for practical hydrogen applications.

Keywords: Hydrous Hydrazine, Hydrogen, Batch reactor, CFD

1. Introduction

Fossil fuels are widely used as the world's main energy source, which led to the emission of green-house gases (GHGs), contributing to climate change and global warming [1]. Carbon dioxide (CO_2) is considered the main GHG, produced by fossil fuels combustion. [2]. To meet the global energy consumption requirements, renewable energy sources have gain interest to accomplish a policy of zero carbon emission [3]. In particular, hydrogen (H_2) is a great alternative since it possesses a low environmental impact and a much higher gravimetric energy content than that of conventional fuels [4].

H_2 is primarily derived from natural gas, oil, and coal but various technologies are emerging to produce H_2, such as nuclear power or renewable sources using solar/wind energy, biomass, geothermal and hydrogen containing compounds [5]. Liquid Organic Hydrogen Carriers (LOHCs) offer a promising solution for hydrogen storage and transport, with advantages including increased capacity, ease of handling, and adaptability to existing infrastructure [6]. Although, they are far more advantageous than traditional methods, harmful carbon-based byproducts and GHGs are nevertheless produced from the organic content. To overcome this obstacle, carbon-free hydrogen carriers are therefore required such as ammonia borane (NH_3BH_3), hydrous hydrazine ($N_2H_4.H_2O$, HH) and hydrazine borane ($N_2H_4BH_3$) [7–13].

Hydrous hydrazine ($N_2H_4.H_2O$, HH) is a very promising hydrogen carriers to achieve mild CO-free H_2 production, due to its high hydrogen content (7.9 wt%) and since it is liquid and stable at standard conditions. The decomposition of HH occurs in two different routes: the complete dehydrogenation pathway (Eq.1), producing hydrogen (H_2) and nitrogen (N_2), and the incomplete dehydrogenation pathway (Eq.2), where the only by-products are ammonia (NH_3) and nitrogen (N_2), which is also the thermodynamically favoured pathway [14].

$$N_2H_4\,(l) \rightarrow 2H_2\,(g) + N_2\,(g),\ \Delta H = -95.4\ kJ/mol \quad (1)$$

$$3N_2H_4\,(l) \rightarrow 4NH_3\,(g) + N_2\,(g),\ \Delta H = -157\ kJ/mol \quad (2)$$

Nowadays, great interest is aimed at developing highly efficient catalytic systems that are selective to H_2. Among several noble and non-noble monometallic systems, it was observed that Rh nanoparticles (NPs) achieved the highest catalytic activity but with a low yield of 43.8%, while non-noble metals weren't active. [15].Supports also play a pivotal role in the development of novel and efficient catalysts. The most used supports are oxides such as aluminium (III) oxide (Al_2O_3), titanium (IV) oxide (TiO_2) and cerium (IV) oxide (CeO_2) due

to strong metal-support interactions modulating the metal electronic structure, thus the structure-activity relationships. Furthermore, when immobilised on the support surface NPs are dispersed and stabilised, thus more accessible to the substrate and less prone to sintering and agglomeration under reaction condition [16]. For the enhancement of the catalytic performance, a second metal can also be introduced to form a bimetallic system, e.g. Rh-Ni catalytic systems [17].

A study by Yao et al. [18] investigated hydrous hydrazine decomposition using a range of Rh-MoOx nanoparticles with different metal compositions. The $Rh_{0.5}(MoOx)_{0.5}$ catalyst was the optimal among all the as-prepared Rh-MoOx NPs, achieving 100% yield towards H_2 and a TOF value of 750 h^{-1} under alkaline conditions. It was concluded that the improved catalytic properties may be ascribed to the MoOx dopant-induced altered electronic structure, low crystallinity, small particle size, and robust basic sites of Rh NPs.

The investigation of HH catalytic decomposition was only reported in batch systems (flasks) so far [19–23], due to their easy set-up and low cost. However, the deactivation of the catalyst cannot be investigated properly in a batch system. The stability of the catalyst can only be studied by introducing equal volumes of reactant solution in the system after the completion of the reaction causing dilution of the reactant, decreasing the total concentration and thus, the reaction rate. However, a batch set-up is necessary because the presence of alkali (NaOH, KOH) is needed for the reaction since it promotes the breakage of the N-H bond instead of the N-N bond and thus the decomposition towards H_2 and N_2 [24–27]. The basic medium used in the reaction could cause corrosion in other systems and eventually destroy them [28].

Motta et al. [29] synthesised iridium catalysts deposited on the cerium oxide surface (1 wt% Ir/CeO_2) for the decomposition of hydrous hydrazine. The catalytic tests took place in a sealed single-neck round bottom flask used as a batch reactor. The decomposition was monitored through a gas collection system with an acid washing bottle (1M HCl) to trap NH_3 if produced. Parameters such as temperature, concentration of the alkali, stirring rate and catalyst to substate molar ratio were modified to study the effect on yield and activity. The optimal conditions were 50 ^oC, 0.5 M of the base, 1050 rpm and 250:1 substrate to metal molar ratio. Performing the reaction on experimental basis is practical but time consuming.

Computational fluid dynamics (CFD) software can thus be utilised since they are a valuable tool that provide accurate validation of the experimental results [30, 31, 40, 32–39]. Besides validation, computational simulations can predict and optimise data, offering the opportunity

for parameter optimisation without any need for repetition of the experiment. CFD modelling has not yet been implemented for the catalytic reaction of HH since the reaction rate of this reaction is complicated and many studies report different decomposition mechanisms and reaction kinetics [41–43].

Aim of this work is to find the optimal experimental conditions for the decomposition of HH, using a commercial 0.5 wt% Rh/Al_2O_3 catalyst and couple the data with computational simulations for validation. To the best of our knowledge, no CFD models were developed combining reaction kinetics data from literature with experimental findings to describe this reaction. With the use of COMSOL Multiphysics, CFD studies on HH decomposition were conducted, performing also CFD parametric studies on the system's uniformity, investigating velocity and temperature fields and distribution of the reactant and the catalytic particles in the system. These results offer a better understanding on parameter optimisation and get better insights for hydrous hydrazine decomposition for carbon-free H_2 production.

2. Experimental Methodology

2.1 Materials

Commercial 0.5% Rh/Al_2O_3 was supplied by Engelhard. Hydrous hydrazine ($N_2H_4{\cdot}H_2O$, 98 %) and sodium hydroxide (NaOH, ≥98 %), were acquired from Sigma-Aldrich.

2.2 Characterization

Transmission electron microscopy (TEM) characterization of the samples was performed using a TEM/STEM FEI Talos F200X G2 microscope (Thermo Fisher Scientific, Waltham, MA, USA). This equipment allows obtaining HAADF-STEM images and XEDS thanks to 4 Super-X SDDs. HAADF-STEM, a technique whose contrast/intensity is sensitive to the square of the atomic number, is particularly suitable for distinguishing highly dispersed nanoparticles of heavy elements such as Rh on light supports like alumina. However, EDXS was recorded to confirm that the contrast corresponds to the Rh nanoparticles.

2.3 Catalytic experiment

A two-necked round bottom flask (35 mL) was used to perform HH decomposition at the desired temperature, under kinetic conditions [44]. One of the flask's necks was connected the *Man On the Moon X102* kit recording the partial pressures of the released gas, as reported in many studies regarding H_2 generation [45–47]. The required amount of catalyst was placed to the reactor, where 5.0 mL of a 0.5 M NaOH aqueous solution was introduced and heated at the desired temperature. After an equilibration of the system, a syringe was used to inject into the

reactor 300 μL of an aqueous solution containing 3.3 M hydrous hydrazine via a vacuum septum. The products evolution was sampled each 0.3s until the reaction reaches a pressure plateau signalling the end of the reaction. To verify experimental reproducibility and evaluate measure uncertainty, all catalytic tests were carried out three times. Equation 3 was used to calculate the yield towards H_2 generation (x):

$$3N_2H_4 \rightarrow 4(1-x)NH_3 + 6xH_2 + (1+2x)N_2 \quad (3)$$

To guarantee the removal of any NH_3, the released gaseous products were allowed to pass through a trap filled with an aqueous solution of 0.05 M HCl [22]. Thus, the measured gas pressure during the reaction was consisted only of N_2 and H_2, enabling to obtain the molar ratio (λ) as $\frac{n(H_2+N_2)}{n(N_2H_4)}$ by utilising the ideal gas law ($pV = nRT$). Hence, H_2 yield was computed utilising Equation 4:

$$x = \frac{3\lambda-1}{8}, \left[\lambda = \frac{n(H_2+N_2)}{n(N_2H_4)} \left(\frac{1}{3} \leq \lambda \leq 3\right)\right] \quad (4)$$

As it can be seen from Eq.4, the yield towards H_2 can reach 100% if the normalised ratio has a value of 3, indicating that NH_3 isn't produced. The ratio of converted substrate to metal moles, normalised with respect to the reaction time (t), was used to calculate the catalytic activity. The initial activity was calculated for time approaching zero ($t \rightarrow 0$). The conversion of $N_2H_4 \cdot H_2O$ was quantified through a Jasco V-730 spectrophotometer, using a 1 cm quartz cell, based on the quantitative reaction of the remaining substrate with 4-dimethylaminobenzaldehyde (4-DMAB) in dilute hydrochloric acid (HCl), resulting in a p-quinone structure that strongly absorbs radiation at 456 nm [48].

3. Modelling Methodology

3.1 Reaction kinetics

The Power-Law model is used to describe the reaction rate of the decomposition of hydrazine as shown below:

$$r = k \times C_1^{n1} \times C_2^{n2} \quad (5)$$

where r denotes the reactants rate expression (mol/m^3.s), k is the specific rate constant (1/s), C_1 and C_2 denote the initial concentration with respect to HH and catalyst (mol/m^3), and lastly n_1 and n_2 are the orders of the reaction for HH and catalyst respectively. A value of 43.3 kJ/mol for the activation energy (E_a) was calculated based on the experiments. The complicacy of this

reaction leads to limited data regarding its kinetics. For the order of reaction regarding HH concentration, an average value of 0.33 was reported by a review study [49] while for the catalyst concentration a value near 1.00 was found [49–52] and thus the order was fixed to 1.00, which validated accurately the experimental data.

3.2 Batch reactor modelling

In a batch reactor there is no inflow or outflow and therefore a sealed, perfectly mixed system of constant volume is assumed. Additional hypotheses are that fluids both in gas and liquid phase are ideal. Based on the above assumptions a zero-dimensional (0D) model was developed utilising the COMSOL 5.6 simulation software.

The mass balance for each component, i, is given by:

$$\frac{d(c_i V_r)}{dt} = V_r R_i \tag{6}$$

where c_i is the molar concentration of each species (mol/m^3), V_r expresses the volume (m^3), t is the time (s) and R_i denotes the sum of each components rate expression (mol/m^3.s). The variation of volume is also included in the Eq.6 and thus, based on the assumptions mentioned above, the mass balance can be expressed as:

$$\frac{dc_i}{dt} = R_i \tag{7}$$

The energy balance for an ideal and incompressible liquid reactant is:

$$V_r \sum_i c_i C_{p,i} \frac{dT}{dt} = Q + Q_{ext} \tag{8}$$

where $C_{p,i}$ is the molar heat capacity for each component (J/mol.K) and T is the temperature (K). On the right side of the equation, Q expresses the chemical reaction heat (J/s) while Q_{ext} presents the heat added to the system (J/s).

The heat of reaction can be calculated by:

$$Q = -V_r \sum_i H_j r_j \tag{9}$$

In the above formula H_j is the molar enthalpy (J/mol) and r_j is the rate of reaction (mol/m^3.s).

For the simulation of the velocity and temperature fields, a 2D model was developed using the Rotating Machinery, Turbulent Flow, k-ε and Heat Transfer in Fluids using both frozen rotor and time-dependent study types. The continuity equation and Navier-Stokes equation are the

183 equations solved by the Turbulent Flow, k-ε interface as shown below, for conservation of mass
184 and for conservation of momentum, respectively.

185 The continuity equation is written as:

186 $$\frac{\partial \rho}{\partial t} + \nabla \cdot (\rho u) = 0 \quad (10)$$

187 where ρ is the density of the fluid (kg/m^3) and u is the velocity (m/s). For an incompressible
188 fluid, the density is constant and therefore the equation becomes:

189 $$\rho \nabla \cdot u = 0 \quad (11)$$

190 The Navier-Stokes equation is:

191 $$\rho \frac{\partial u}{\partial t} + \rho(u \cdot \nabla) = \nabla[-pI + \kappa] + F \quad (12)$$

192 where on the right hand of the equation, p is the pressure (Pa), I denotes the identity tensor, F
193 is the external force (N/m^3) and κ is the viscous stress tensor (Pa) and describing an
194 incompressible Newtonian fluid gives:

195 $$\kappa = (\mu + \mu_T)(\nabla u + (\nabla u)^T) \quad (13)$$

196 where μ is the dynamic viscosity (Pa.s) and μ_T is the turbulent viscosity given by the equation
197 below:

198 $$\mu_T = \rho C_\mu \frac{k^2}{\varepsilon} \quad (14)$$

199 where C_μ is a model constant, k is the turbulent kinetic energy (m^2/s^2) and ε is the turbulence
200 dissipation rate (m^2/s^3).

201 The model introduces two additional transport equations for the two dependent variables, k
202 and ε:

203 The transport equation for k is:

204 $$\rho \frac{\partial k}{\partial t} + \rho(u \cdot \nabla)k = \nabla \cdot \left[\left(\mu + \frac{\mu_T}{\sigma_k}\right)\nabla k\right] + P_k - \rho\varepsilon \quad (15)$$

205 with P_k a production term of:

206 $$P_k = \mu_T[\nabla u : (\nabla u + (\nabla u)^T)] \quad (16)$$

207 The transport formula for ε is:

$$\rho\frac{\partial\varepsilon}{\partial t}+\rho(u\cdot\nabla)\varepsilon=\nabla\cdot\left[\left(\mu+\frac{\mu_T}{\sigma_\varepsilon}\right)\nabla\varepsilon\right]+C_{\varepsilon1}\frac{\varepsilon}{k}P_k-C_{\varepsilon2}\rho\frac{\varepsilon^2}{k} \quad (17)$$

Values for the model constants, C_μ, σ_k, σ_ε, $C_{\varepsilon1}$, $C_{\varepsilon2}$, are given from experimental data with values of 0.09, 1.0, 1.3, 1.44 and 1.92 respectively.

The Heat Transfer in Fluids is described by the following energy balance formula:

$$\rho C_p\frac{\partial T}{\partial t}+\rho C_p(u\cdot\nabla T)+\nabla q=Q+Q_p+Q_{vd} \quad (18)$$

where C_p is the heat capacity at constant pressure (J/kg.K) and q is the heat flux by conduction (W/m^2). On the other hand of the formula, Q is the additional heat sources (W/m^3), Q_p is the work done by pressure changes (W/m^3) and Q_{vd} is the viscous dissipation term (W/m^3). The term q is given by Fourier's law of heat conduction as shown below:

$$q=-k\nabla T \quad (19)$$

where k is the thermal conductivity (W/m.K).

Additionally, the dispersion of hydrazine and catalytic particles was simulated using the Transport of Diluted Species Physics Interface and the Particle Tracing for Fluid Flow respectively. The Transport of Diluted Species was solved using the Fick's law equation:

$$\frac{\partial c_i}{\partial t}+\nabla\cdot J_i+u\cdot\nabla c_i=R_i \quad (20)$$

where J_i is the diffusion flux (mol/(m^2.s) given by:

$$J_i=-D_i\nabla c_i \quad (21)$$

where D_i is the diffusion coefficient (m^2/s).

For the distribution of the particles the Newtonian formulation is used, based on Newton's second law of motion:

$$\frac{d}{dt}\left(m_p\frac{dq}{dt}\right)=F \quad (22)$$

where m_p is the particle mass (kg), q is the position of the particle (m) and F is the total force on the particles (N).

For this simulation, an alteration of the Eq.22 was used, the Newtonian first-order formulation as shown in below:

$$\frac{d(m_p v)}{dt} = F \quad (23)$$

where v is the particle velocity (m/s) equal to $\frac{dq}{dt}$.

The particles are reflected when hitting the reactor walls with a velocity of:

$$v = v_c - 2(n \cdot v_c)n \quad (24)$$

where v_c is the particle velocity when hitting the wall and n the incident/reflected angle.

For this work, COMSOL Multiphysics 5.6 was used, utilising the feature Reaction Engineering of the Chemical Reaction Engineering module to develop a batch reactor for the decomposition of hydrazine. The batch system had 4 degrees of freedom and an average of 5 s of computational time. For the 2D system Rotating Machinery, Turbulent Flow, k-ε, Heat Transfer in Fluids, Transport of Diluted Species and Particle Tracing for Fluid Flow interfaces were used with 32486, 6452, 6498 and 20001 degrees of freedom and 27 min, 1 min, 22 min and 1 min computational time respectively.

4. Results and Discussion

4.1 Catalyst characterisation

The commercial 0.5% Rh/Al2O3 catalyst was characterized utilising transmission electron microscopy, as illustrated in Figure 1. Our comprehensive analysis reveals that Rh nanoparticles are uniformly dispersed across the alumina support. Analysis of the particle size distribution included in Figure 1c reveals a predominantly unimodal distribution and an average particle size of 2.46 nm. The particle size distribution was also employed to determinate the particle dispersion. This result indicates that the catalyst exhibits a notable level of particle dispersion, approximately 42%, highlighting the effectiveness of the catalyst preparation method in achieving uniform nanoparticle distribution. In agreement with the TEM analysis, because of the low metal loading, the XRD pattern (Figure S1) did not reveal any signal of crystalline Rh, confirming the presence of small, well-dispersed particles over the support.

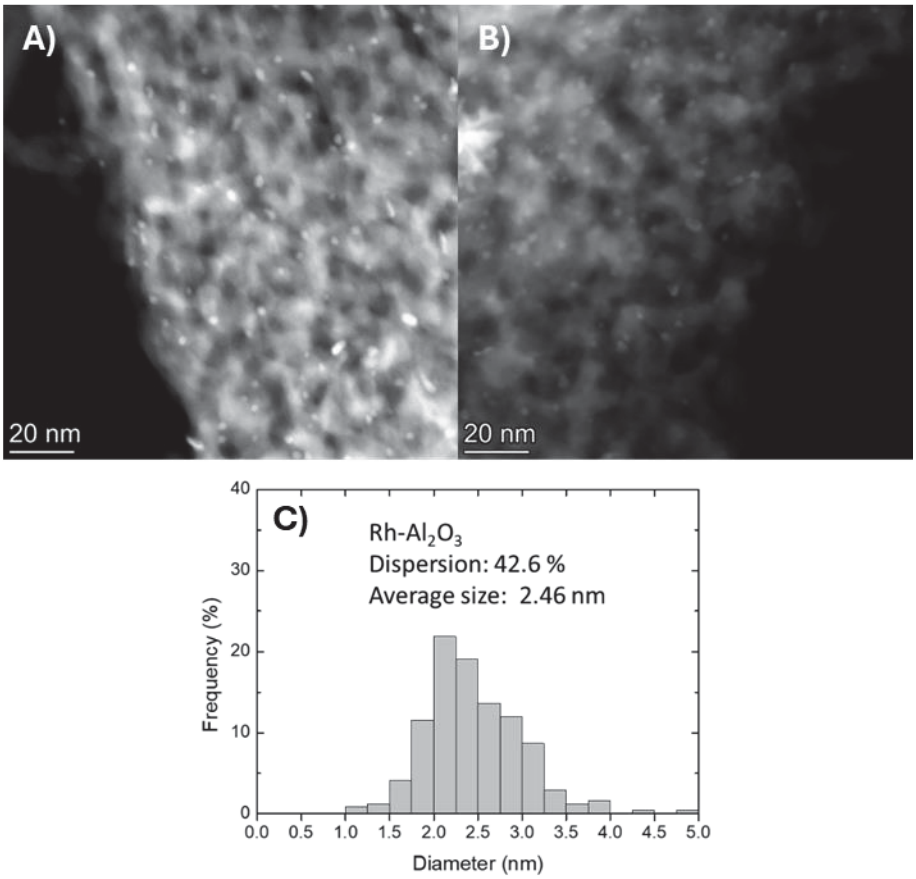

Figure 1. HAADF images and particle distribution of commercial Rh/Al_2O_3.

4.1.1 Catalytic tests

Catalytic tests were performed varying parameters that are known to have an effect either on the yield of the reaction, catalytic activity, or both. Stirring rate, temperature, mass of catalyst, N_2H_4 concentration and NaOH concentration were investigated to find the ideal experimental conditions for maximum H_2 generation and provide a power-law rate expression to describe the decomposition of HH. Hydrous hydrazine decomposition was conducted in batch reactor and the kinetic profiles are evaluated in terms of the normalised ratio of $n(H_2+N_2)/n(N_2H_4)$ plotted against the reaction time to highlight H_2 generation. Complete conversion was verified through the UV-Vis analysis of hydrous hydrazine quantitatively reacted with 4-DMAB. The yield to H_2 was evaluated using the pressure of the gaseous products (H_2 + N_2). Based on the stoichiometry of the reaction, at complete conversion, a 100 % H_2 yield corresponds to a $n(H_2+N_2)/n(N_2H_4)$ value of 3, while of 0.3 corresponds to 0 %.

CFD studies were, afterwards, implemented using the experimental data and kinetics from literature to compare the predicted values with the experimental results, investigating the accuracy of the model. The combination of the experimental and computational parametric studies is presented below.

4.1.1.1 Effect of stirring rate

External mass transfer limitations can occur related to the diffusion of the reactant from the liquid bulk on the external surface of the catalytic particle, depending on the thickness of the boundary layer in between of the liquid and the catalyst surface [53]. Therefore, it is essential to confirm that the reaction is kinetically controlled. Internal mass transfer limitations can be neglected since the catalyst is in powder form. Catalytic tests took place changing the stirring rate from 250 to 1400 rpm. From Figure 2, it is observed that the stirring rate has no substantial effect on the yield of the reaction. CFD studies agree with the experimental results since the stirring rate is only expected to influence the diffusion. Indeed, comparing the TOF values from the different stirring rates (Figure 3), it is evident that at lower stirring rates the catalytic activity is lower, while a plateau is reached between the values of 750 and 1400 rpm. Thus, mass transfer resistance is avoided since TOF values above 750 rpm are constant. Other studies also confirmed that the reaction is not controlled by mass transfer above 900 rpm and at stirring rates below 300 rpm, mass transfer resistances influence the reaction rate [54, 55]. Further experiments were conducted under 1400 rpm to ensure the achievement of kinetic regimes.

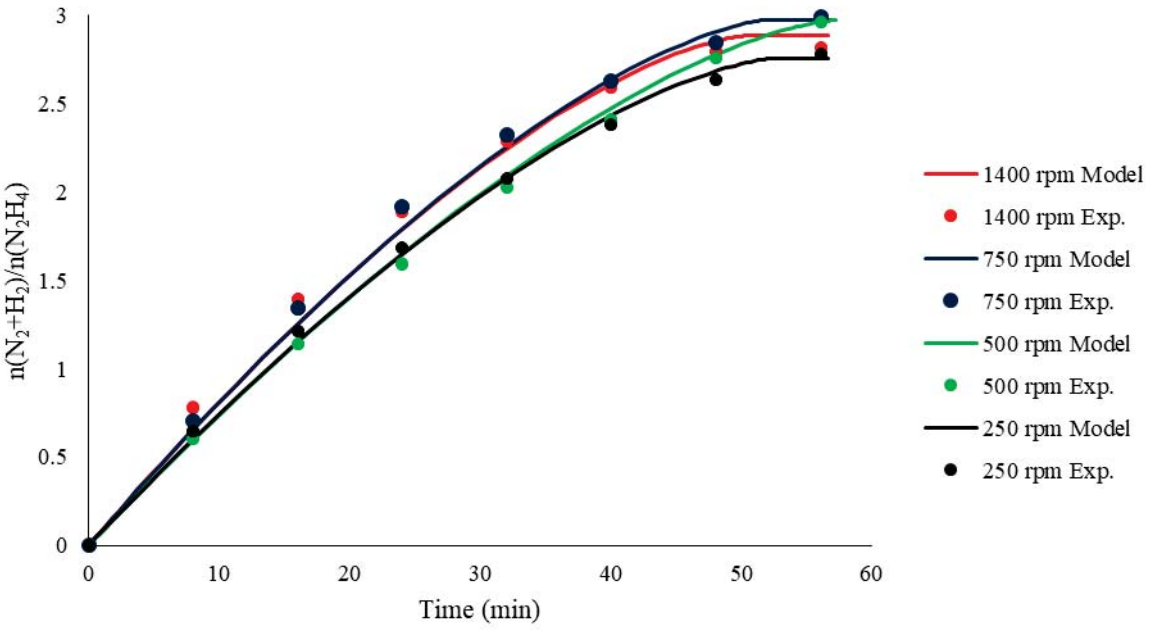

306 **Figure 2.** $n(H_2 + N_2)/n(N_2H_4)$ versus time varying the value of stirring rate at 250, 500, 750
307 and 1400 rpm. Reaction conditions: 150 µL of 3.3 M N_2H_4, 0.5 M NaOH, 1000:1 substrate to
308 metal molar ratio and temperature of 70 ºC.

309
310
311
312
313
314
315
316

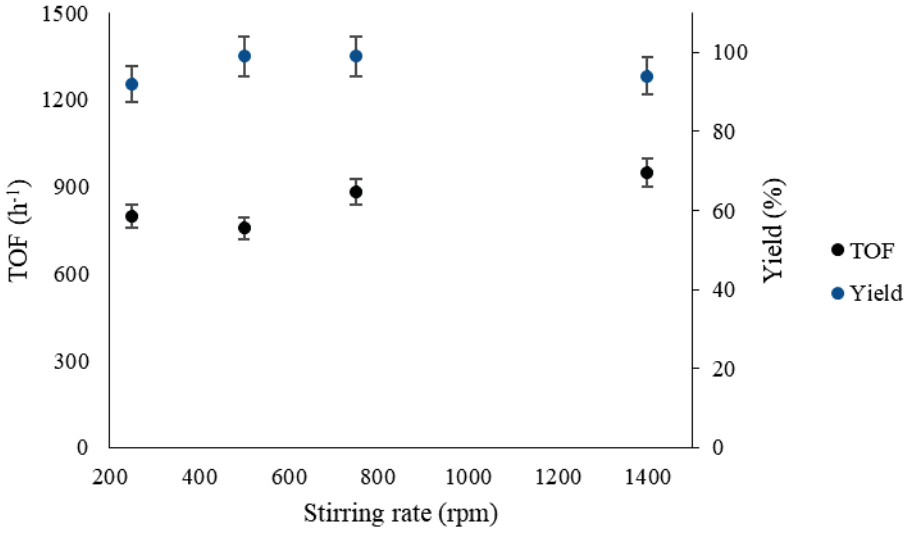

317 **Figure 3**. TOF (left y–axis), and yield (right y–axis), at different stirring rates.

318

To ensure the uniformity of the system and the avoidance of external mass transfer limitations, a 2D simulation was developed investigating the velocity magnitude at 1400 rpm. As seen from Figure 4, the initial velocity distribution is not uniform in the batch system (Figure 4a). Moving to 0.25 and 0.5 s (Figure 4b and c, respectively) the velocity field starts to appear smoother. Uniformity of the system is achieved at 0.75s and remains constant with the stirring. The highest velocity magnitude can be observed at the top and bottom of the magnetic stirrer as expected, since it is the area that the fluid hits the stirrer resulting in higher velocity, while the remaining surface area has an average velocity magnitude. The simulation findings are in a great agreement with the expectations, considering the small size of the batch reactor and high rotational rate utilised.

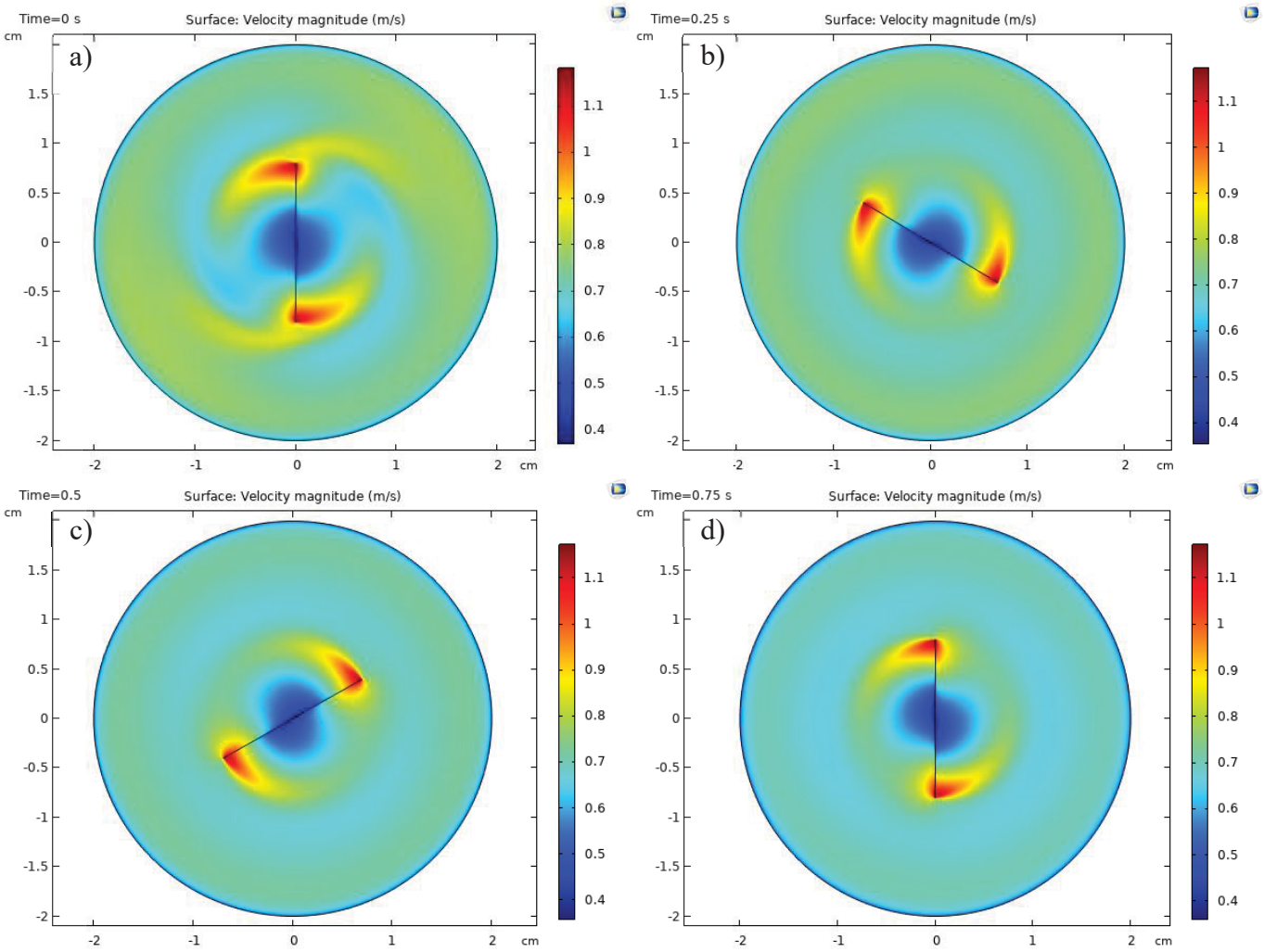

Figure 4. Velocity field distribution at 1400 rpm in the batch system over time at a) 0s, b) 0.25s, c) 0.5s and d) 0.75s.

It is known that low rotational rates will cause a non-uniform distribution of the solution. Thus, CFD analysis was also conducted with lower stirring rates (250, 500 and 750 rpm), according to the experiments, to show how the solution is dispersed in the batch system. From Figure 5 below, it is evident that at 250 rpm, the solution is not well mixed far from the magnetic stirrer. At 450 rpm the mixing is improved, but still the rate is very low. Using 750 rpm, the velocity field distribution is similar with the 1400 rpm, confirming the kinetic regime validation from the TOF analysis. Lower velocity range, compared to 1400 rpm, is also observed at every case of lower stirring rate and thus, 1400 rpm was the optimal stirring rate. Since, there was a good validation between the 2D simulation and the experimental findings regarding the rotational speed, the effect of the magnetic stirrer dimension was also studied computationally. Figure S2 provides the velocity profile when a smaller stirrer is used. The size of the stirrer prevents the solution from being evenly mixed over the reactor's radial surface, creating a "dead zone." Conversely, when a bigger magnetic stirrer is used, the "dead zone" is near the stirrer, but the rest of the reactor surface is uniform (Figure S3). However, when big stirrers are used in experiments at high speeds, droplets of the solution are formed on the walls wasting a substantial amount of the reactant and catalyst.

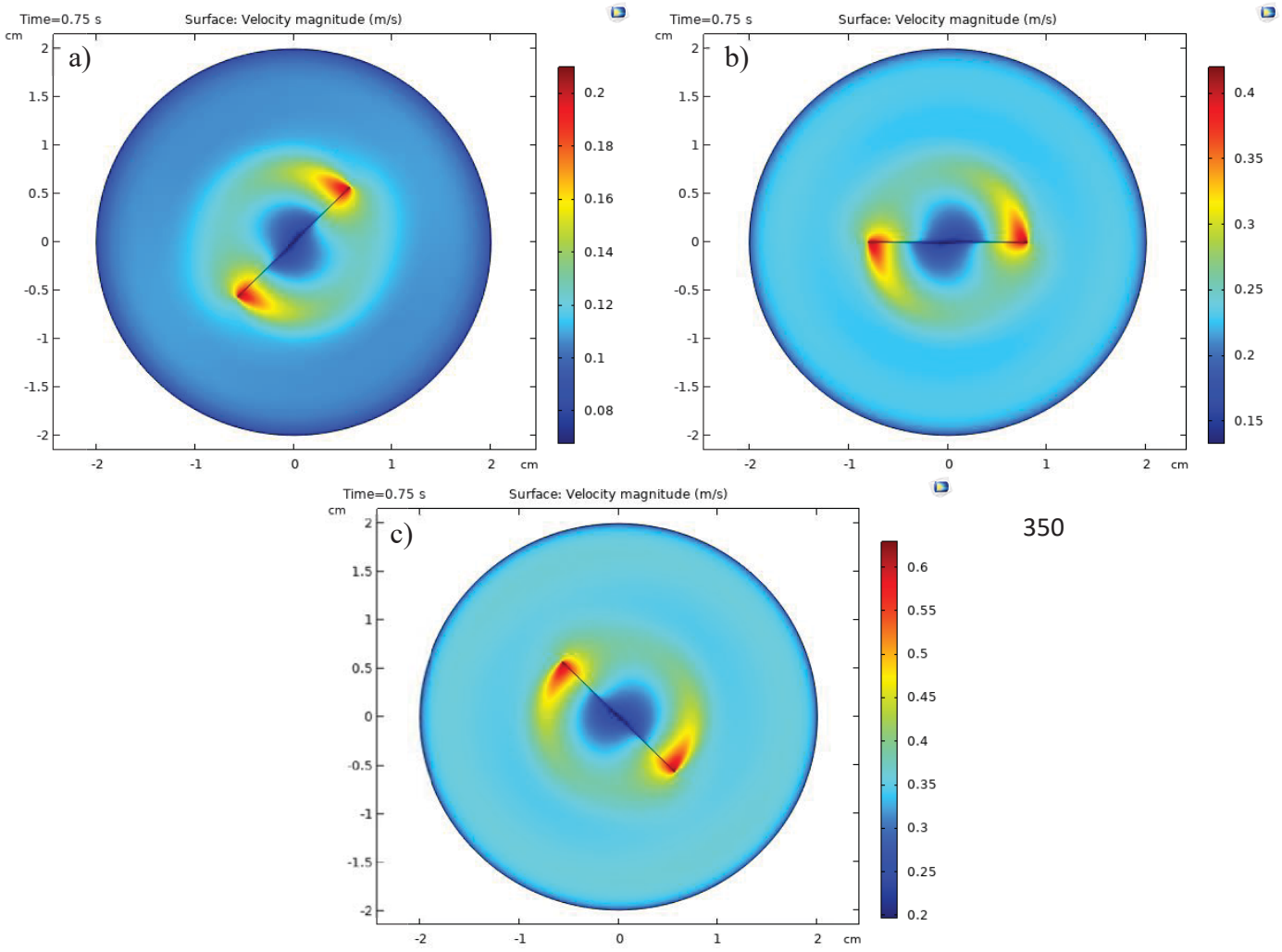

350

Figure 5. Velocity field distribution in the batch system at a) 250 rpm, b) 500 rpm and c) 750 rpm.

It is evident form the above experimental and simulation results, that 1400 rpm is the optimum stirring rate. Indeed, based on the further conducted CFD studies the external mass transfer cannot be neglected at low stirring rates since low velocity implying that an interface of relatively large thickness, that the reactant must diffuse through to get to the surface of the catalyst. The stirrer length that was also examined computationally, demonstrated that the size of the stirrer has a significant effect on the velocity field enhancing the need of CFD studies for time-saving results.

4.1.1.2 Effect of temperature

The temperature is a significant parameter since it affects the yield of the reaction. Indeed, the pathway towards H_2 production is more endothermic (ΔH = -95.4 kJ/mol) compared with the reaction generating NH_3 (ΔH = -157 kJ/mol) and thus favoured in higher temperatures, meaning that at lower temperatures NH_3 will be the main product of the reaction. However, it is reported by many studies that even though the increase of the temperature favours the decomposition towards H_2, higher temperatures might result in a decreased yield. This could be a result of reaction intermediates that occur at higher temperatures causing the poisoning/saturation of the active sites. In the case of the commercial Rh/Al_2O_3 increasing the temperature from 50 to 70 ºC the yield increases up to 93% (Figure 6), and at 80 ºC the yield of H_2 is decreased but the activity of the catalyst is increased (Figure S4). Therefore 70 ºC was chosen as the optimised temperature even though the maximum yield reached is 93%, meaning that NH_3 or reaction intermediates are also generated. The computational results agree with the experimental data, proving again that the kinetic data obtained from literature describe accurately the decomposition reaction rate. An Arrhenius plot is also presented below (Figure 7) where the E_a was calculated at 43.3 kJ/mol.

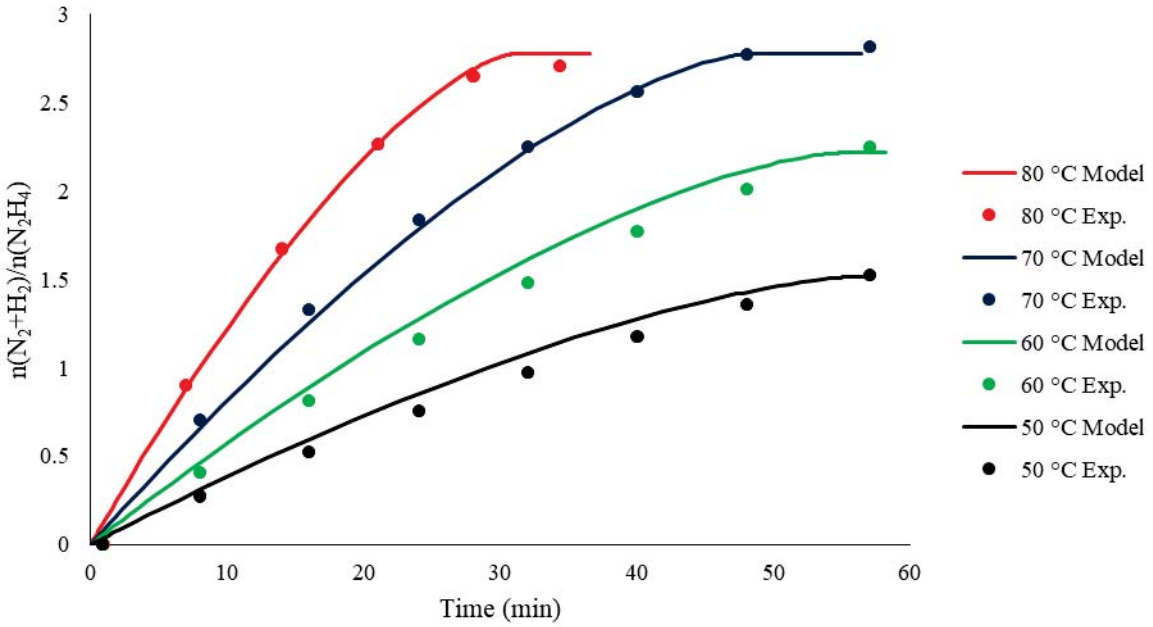

Figure 6. $n(H_2 + N_2)/n(N_2H_4)$ versus time at temperatures of 50, 60, 70 and 80 ºC. Reaction conditions: 150 μL of 3.3 M N_2H_4, 0.5 M NaOH, 1000:1 substrate to metal molar ratio and 1400 rpm stirring rate.

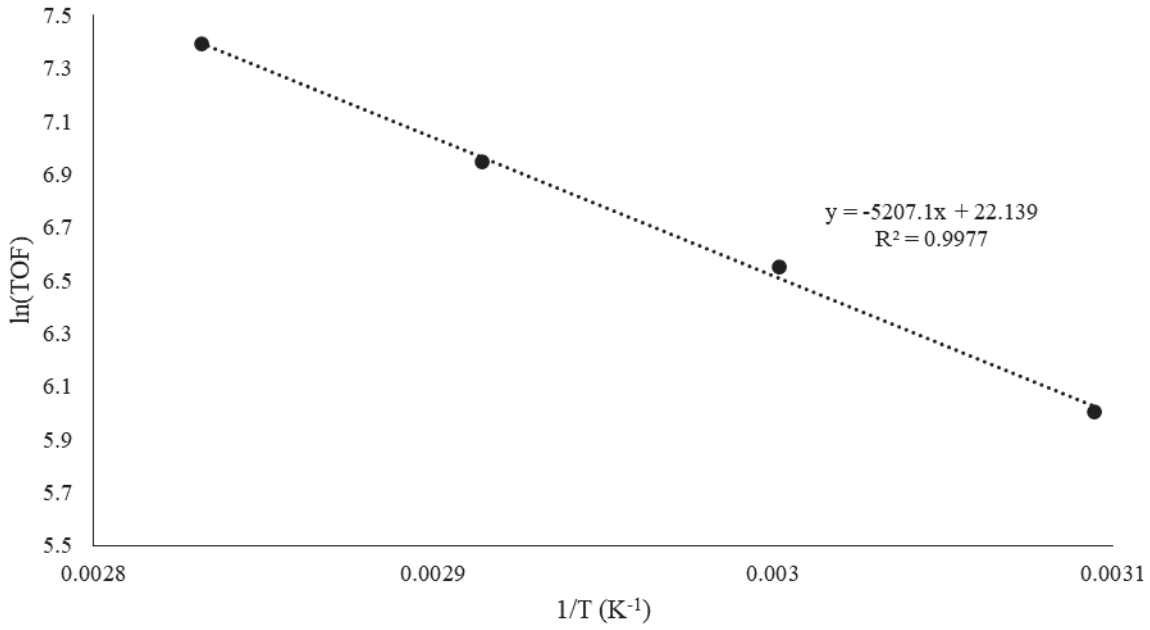

388 **Figure 7.** Arrhenius plot (50-80 ºC). Reaction conditions: 150 µL of 3.3 M N_2H_4, 1000:1
389 substrate to metal molar ratio, 0.5 M NaOH and 1400 rpm stirring rate.

390 The temperature of the reaction is of significance importance as mentioned before. Therefore,
391 computational evaluation of the temperature in the system was also investigated in a 2D model,
392 using the optimum temperature of 70 ºC, at 1400 rpm (Figure 8). As seen from Figure 8a at
393 time zero the reactor is at room temperature and only the external part of the reactor has the set
394 temperature. A total of 25 minutes are needed for the temperature of 70 ºC to reach the centre
395 of the reactor showing a homogeneous temperature distribution. Thus, it is evident that the
396 reactor is isothermal, and the reaction takes place at 70 ºC with no hot spots observed in the
397 system.

398

399

400

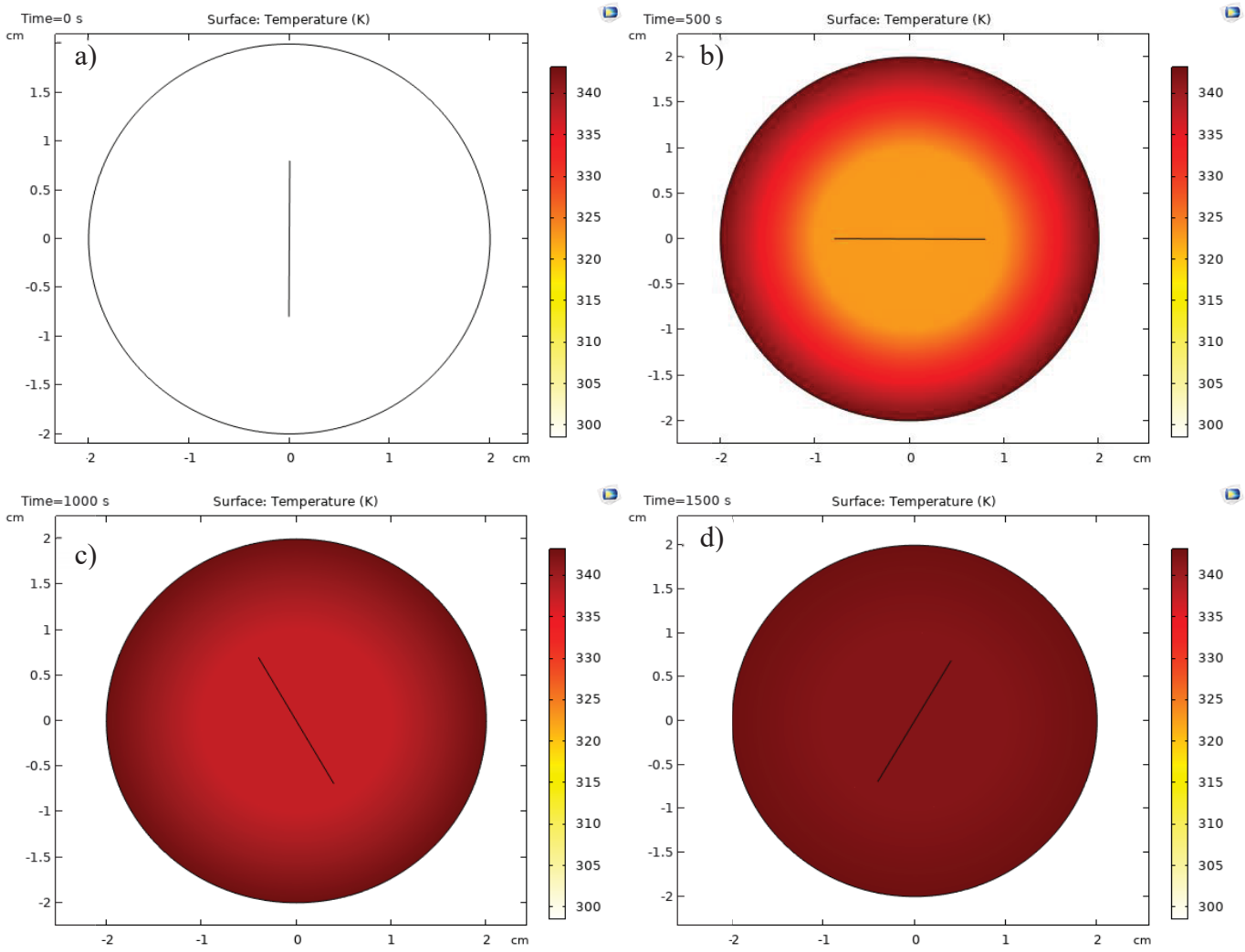

401 **Figure 8.** Temperature distribution in the batch system over time at a) 0s, b) 500s, c) 1000s and
402 d) 1500s, with stirring rate of 1400 rpm.

403 As expected, high temperatures favour the generation of H_2. Both experimental data and
404 simulation studies were in a good agreement with the simulation studies, showing that
405 increasing the temperature the yield is also increasing up to a limit where reaction intermediates
406 are generating. Moreover, the CFD studies predicted that the total time needed to achieve an
407 isothermal temperature distribution is 25 minutes, giving significant information for the
408 catalytic experiments such as the need to wait 25 minutes before adding the reactant, to ensure
409 a homogeneous temperature distribution.

410 4.1.1.3 Effect of mass of catalyst

411 Catalytic tests with different substrate to metal molar ratios were performed to test a possible
412 effect of the mass of catalyst, in the H_2 yield and on the mass transfer. Ratios of 4000:1, 2000:1,
413 1000:1 and 500:1 were used (0.0023, 0.0047, 0.0095 and 0.019 g of catalyst respectively). As

it can be seen from Figure 9 increasing the amount of metal, there is an increase in the yield of H_2 and activity. Lower catalyst concentrations results in yield below 70%. The possible reason behind this is that the substrate concentration is higher compared with the concentration of the catalyst. Thus, the active sites become saturated very quickly and due to the fast release of gases that block the active sites, the available substrate does not react. Moreover, the CFD study is in great agreement with the data obtained from the experiments, achieving higher generation of H_2 when increasing the amount of catalyst. TOF values were calculated (Figure 10) showing that the initial activity was similar for every ratio used. Thus, the constant TOF values confirm that there are no diffusion limitations, and the reaction is kinetically controlled.[29] Even though the 500:1 molar ratio exhibited the highest H_2 yield in less reaction time it wasn't chosen as the optimum ratio due to the need of high amounts of catalyst that would prevent any further experiments and thus the 1000:1 was utilised.

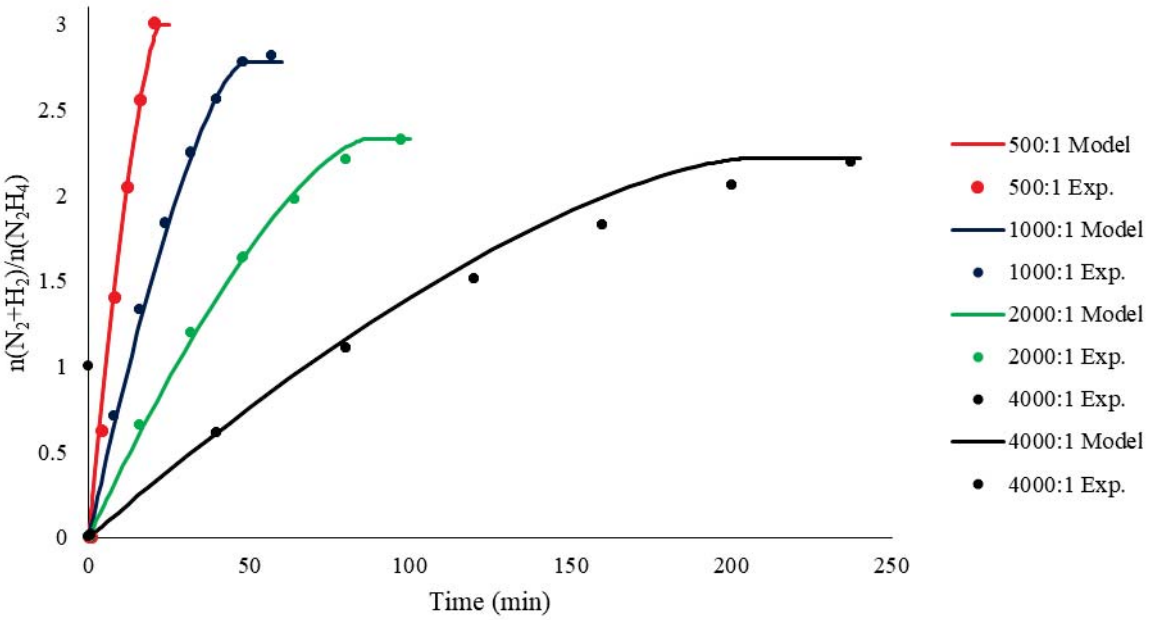

Figure 9. $n(H_2 + N_2)/n(N_2H_4)$ versus time at substrate to catalyst molar ratios of 4000:1, 2000:1, 1000:1 and 500:1. Reaction conditions: 150 μL of 3.3 M N_2H_4, 0.5 M NaOH, 1400 rpm stirring rate and temperature of 70 °C.

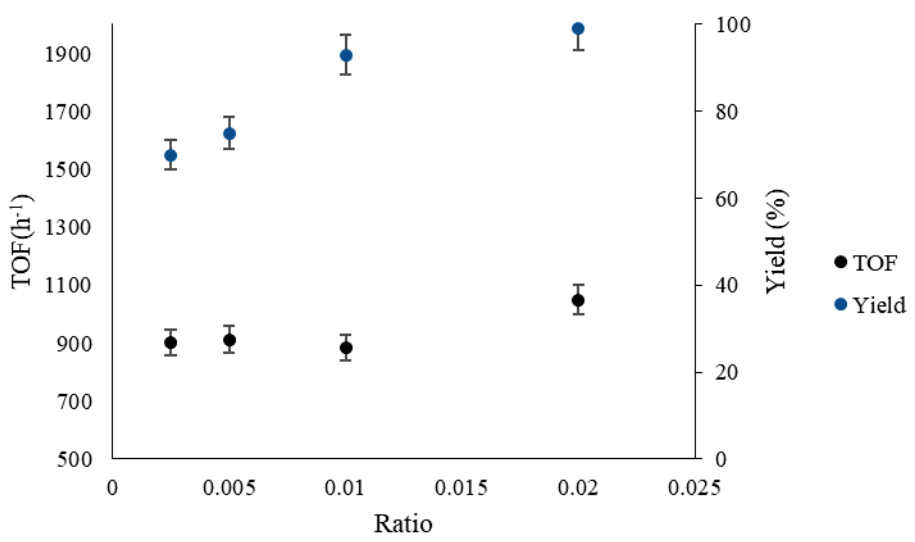

Figure 10. TOF (left y–axis), and yield (right y–axis), at different catalyst mass.

4.1.1.4 Effect of N_2H_4 concentration

Different initial concentrations of the reactant, N_2H_4, were tested to examine the impact of hydrazine concentration on the H_2 yield and to the reaction rate. Concentrations of 0.1 M and below were used to investigate the catalytic performance on low reactants concentration. As it can be seen from Figures 11 and S5, yield increases proportionally up to a certain level and then levels off. For 0.1 M and 0.05 M the yield of the reaction is over 99 and 84 % respectively and therefore lower concentrations can be utilised. Only at 0.025 M the final H_2 yield is extremely low (23%). A possible reason that the normalised ratio $n(H_2 + N_2)/n(N_2H_4)$, does not reach the maximum value of 3 at the lower concentrations of 0.025 and 0.05 M is the complexity of the reaction mechanism. When HH is adsorbed on the catalytic surface, it follows different paths of dehydrogenation, intermolecular dehydrogenation or N-N dissociation, producing adsorbed ions [56]. Due to the low concentrations utilised, the number of ions were insufficient to generate H_2. Another reason might be the occupation of active sites by OH^- ions [42] besides $N_2H_4.H_2O$ molecules, resulting either from water or the NaOH solution. Thus, the low availability of HH can be a limiting factor. It is evident that higher reactant concentrations result in higher generation of H_2. The catalytic activity is also increased by increasing the initial concentration of N_2H_4 (Figure S5) because more substrate is available to take over the active sites of the catalyst. Simulations for the effect of hydrazine concentration were developed with a reaction order of 0.33 [49], exhibiting a good agreement with the catalytic tests.

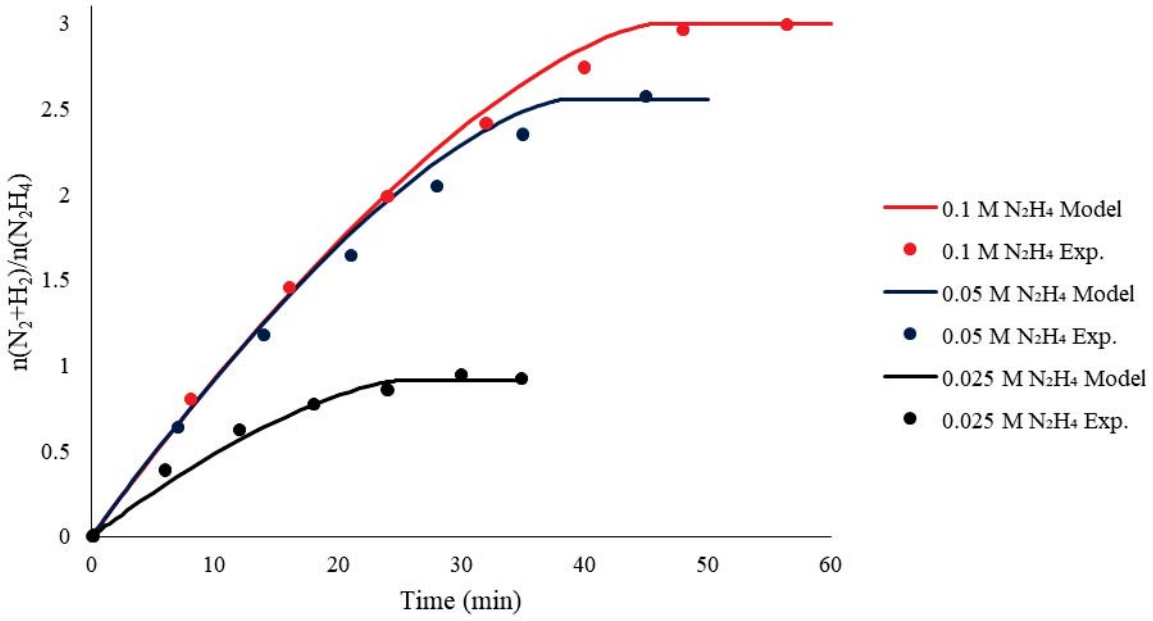

Figure 11. $n(H_2 + N_2)/n(N_2H_4)$ versus time at N_2H_4 concentrations of 0.025, 0.05 and 0.1 M. Reaction conditions: 0.5 M NaOH, 1000:1 substrate to metal molar ratio, 1400 rpm stirring rate and temperature of 70 ºC.

4.1.1.5 Effect of NaOH

The last parameter that was tested was the NaOH concentration. The presence of an alkali in the reaction system is beneficial as reported by many studies [57–60]. As it was mentioned before, the second reaction pathway (Eq.2) is more thermodynamically favourable and thus the breakage of the N-N bond leads to NH_3 production. Moreover, because of N_2H_4 ionisation in water, the protonated form of hydrazine is generated ($N_2H_4 + H_2O \rightarrow N_2H_5^+ + OH^-$) that again can lead to the formation of NH_3. By adding alkali, the formation of undesired $N_2H_5^+$ is suppressed, and the cleavage of the N-H bond is instead favoured leading to the complete decomposition towards H_2 and N_2[61, 62]. In agreement with the literature, in Figure 12, it is clear that the addition of NaOH results in an increase of the yield from 25 to over 80 %. Moreover, NaOH also has an influence on the TOF (732 h^{-1} in water vs. 1280 h^{-1} in NaOH 0.5 M, Figure S6). CFD calculations validated the experimental findings accurately, confirming the promoting effect of NaOH in the system, with the concentration of 0.5 M chosen as the optimum.

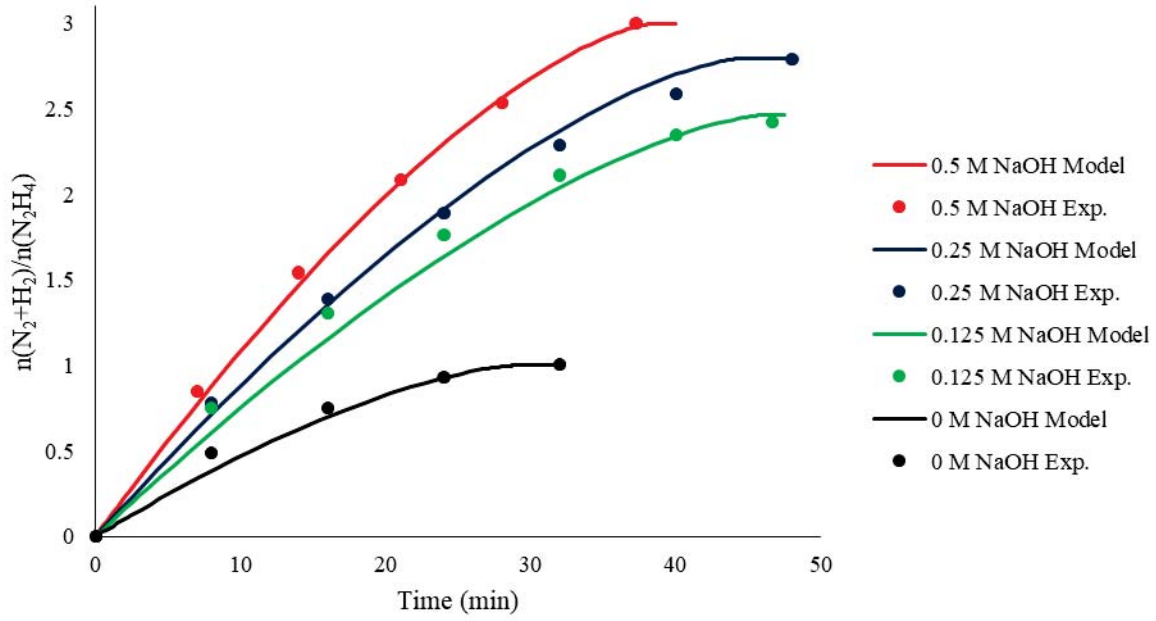

Figure 12. $n(H_2 + N_2)/n(N_2H_4)$ versus time at NaOH concentrations of 0, 0.125, 0.25 and 0.5 M. Reaction conditions: 150 µL of 3.3 M N_2H_4, 1000:1 substrate to metal molar ratio, 1400 rpm stirring rate and temperature of 70 ºC.

4.1.2 N_2H_4 dispersion in the batch reactor

To ensure that $N_2H_4.H_2O$ is well dispersed in the system, the injection point of the solution was modelled to show the mixing process. The point of the injection is near the stirrer but not directly at it to avoid droplets at the walls of the reactor. It is clear that as soon as the injection takes place, $N_2H_4.H_2O$ follows the rotational flow of the NaOH solution in the reactor (Figure 13a). Since it is a very small amount injected and the rotational speed of the stirrer very high it can be seen from the graphs that at 0.34 s the solution is homogeneously dispersed in the reactor.

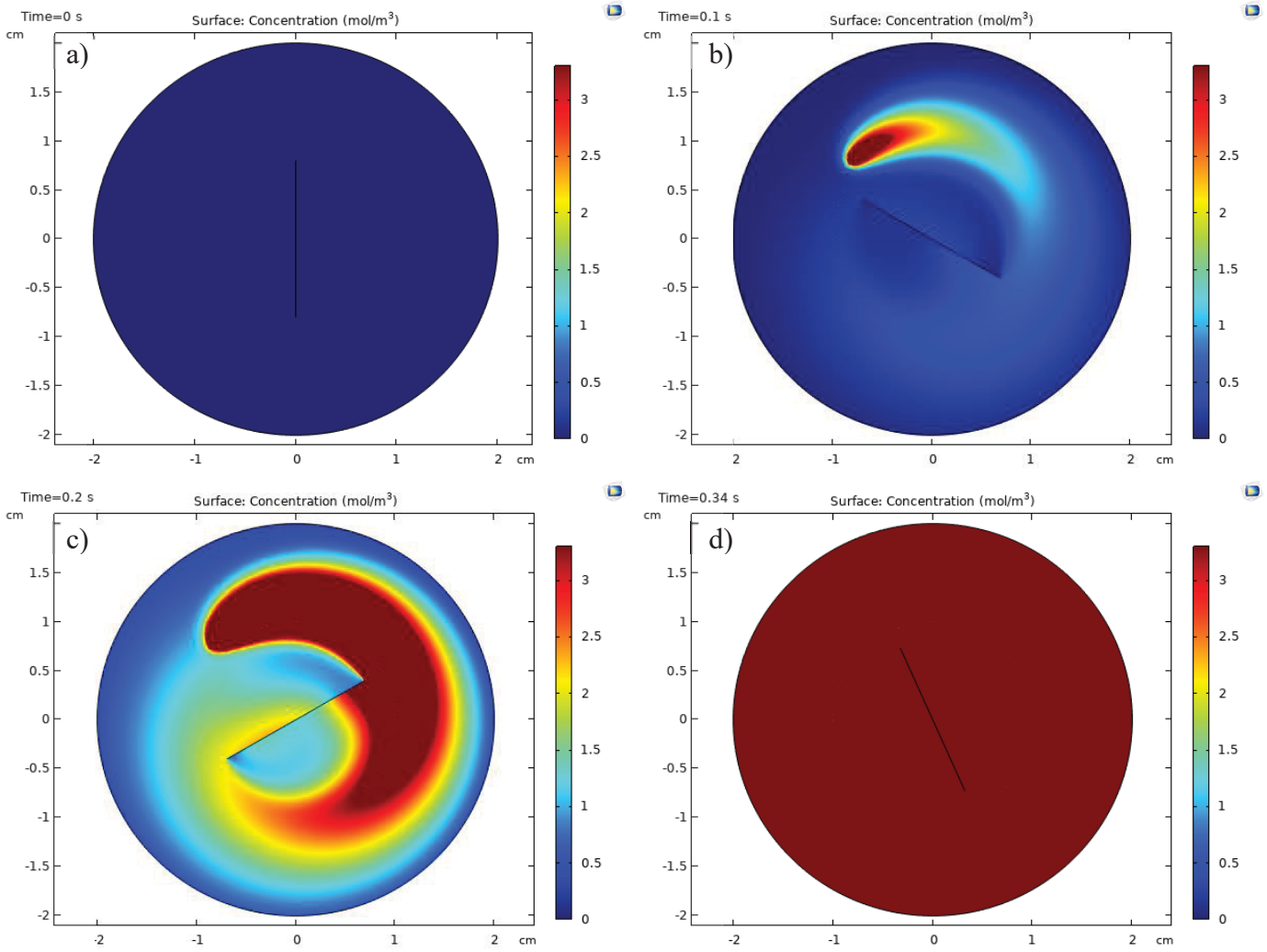

Figure 13. $N_2H_4.H_2O$ distribution in the batch system over time at a) 0s, b) 0.1s, c) 0.2s and d) 0.34s.

4.1.3 Particle trajectories

The position of the catalytic particles is also of significant importance. The more distributed they are in the system, the higher the chance is to adsorb the reactant, $N_2H_4.H_2O$ in this case. Therefore, CFD modelling was employed to track the mixing of the catalytic particles. At zero time there are no particles, yet, in the system (Figure 14a). When they are added, they follow the fluid flow inside the reactor. As soon as they hit the magnetic stirrer bar or the walls they bounce and distributed everywhere in the reactor. After 0.5s, a good mixing of the particles in the system is observed due to the efficient rotation given by the stirrer.

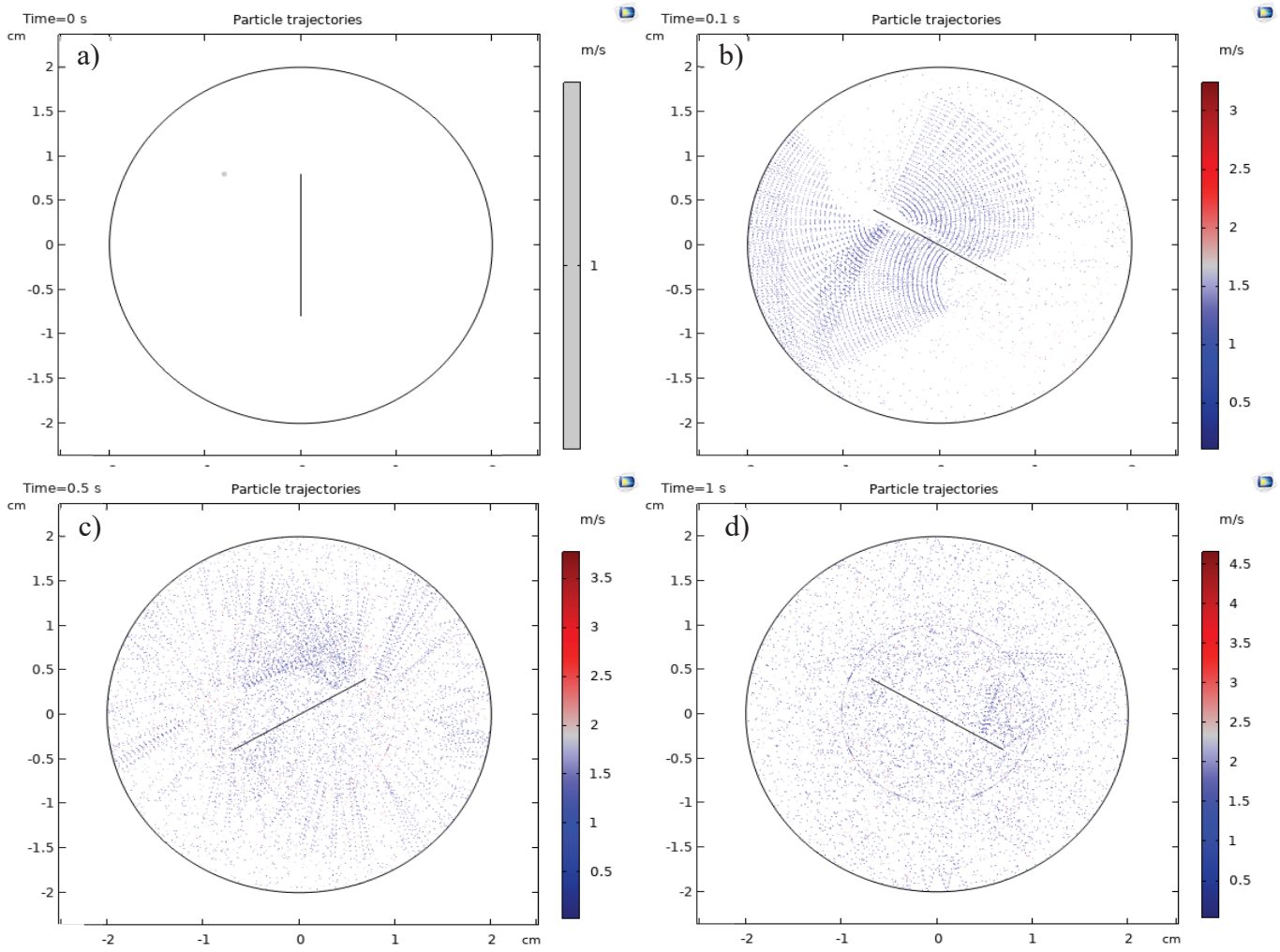

506

507 **Figure 14.** Particle trajectories in the batch system over time at a) 0s, b) 0.1s, c) 0.5s and d)
508 1s.

509 Based on the studies above, the optimised experimental conditions are stirring rate of 1400
510 rpm, temperature of 70 ºC, 1000:1 catalyst to substrate molar ratio, 3.3 M N_2H_4 concentration
511 and 0.5 M NaOH concentration. The computational model built upon the experimental work
512 and kinetic data found in bibliography, validated the experimental findings. Thus, by coupling
513 experimental data with CFD studies, a better understanding of parameter optimisation for the
514 studied reaction can be achieved. Extra CFD studies showed how important is for a system to
515 achieve uniform velocity and temperature distribution for maximum efficiency and confirmed
516 that the particles and hydrazine are indeed homogenously dispersed within the system. Thus,
517 since the simulation accurately represents the decomposition reaction, CFD studies can be
518 further developed for more complex catalytic systems saving time from time-consuming
519 experiments.

520

Conclusions

In conclusion, this study investigated the catalytic decomposition of hydrous hydrazine for H_2 production, emphasising the importance of combination of experimental work and CFD studies. The comprehensive analysis explored the impact of stirring rate, temperature, catalyst mass, hydrazine concentration, and NaOH additions on reaction kinetics and yield. The experimental data, supported by CFD modelling, identified optimal conditions for the decomposition using the Rh/Al_2O_3 catalyst. CFD simulation did not only validated experimental outcomes but also provided a comprehensive understanding of the system's uniformity, including velocity and temperature field distributions and dispersion of hydrazine and particles in the batch system. These collective findings significantly contribute to the application of hydrazine in the field of catalytic H_2 generation, offering a promising pathway for sustainable energy solutions.

CRediT authorship contribution statement

Panayiota Adamou: Writing-Original Draft, Investigation, Formal analysis, Validation. **Silvio Bellomi:** Investigation, Formal analysis, Writing-Review & Editing. **Eleana Harkou:** Writing-Review & Editing. **Xiaowei Chen:** Formal analysis, Investigation, Writing-Review & Editing. **Juan J. Delgado:** Formal analysis, Investigation, Writing-Review & Editing. **Nikolaos Dimitratos:** Writing-Review & Editing. **George Manos** Writing-Review & Editing. **Alberto Villa:** Investigation, Formal analysis, Writing-Review & Editing. **Achilleas Constantinou:** Conceptualisation, Writing-Review & Editing, Supervision.

Declaration of Competing Interest

The authors declare that they have no known competing financial interests or personal relationships that could have appeared to influence the work reported in this paper.

References

1. Hou H, Lu W, Liu B, Hassanein Z, Mahmood H, Khalid S (2023) Exploring the Role of Fossil Fuels and Renewable Energy in Determining Environmental Sustainability: Evidence from OECD Countries. Sustain 2023, Vol 15, Page 2048 15:2048. https://doi.org/10.3390/SU15032048

2. Karakurt I, Aydin G (2023) Development of regression models to forecast the CO2 emissions from fossil fuels in the BRICS and MINT countries. Energy 263:125650. https://doi.org/10.1016/J.ENERGY.2022.125650

3. Zheng J, Du J, Wang B, Klemeš JJ, Liao Q, Liang Y (2023) A hybrid framework for forecasting power generation of multiple renewable energy sources. Renew Sustain Energy Rev 172:113046. https://doi.org/10.1016/J.RSER.2022.113046

4. Azad AK; K;, Rasul MG;, Doppalapudi AT, Kumar Sarker A, Kalam Azad A, Rasul MG, Doppalapudi AT (2023) Prospect of Green Hydrogen Generation from Hybrid Renewable Energy Sources: A Review. Energies 2023 16:1556. https://doi.org/10.3390/EN16031556

5. Hassan Q, Abdulateef AM, Hafedh SA, Al-samari A, Abdulateef J, Sameen AZ, Salman HM, Al-Jiboory AK, Wieteska S, Jaszczur M (2023) Renewable energy-to-green hydrogen: A review of main resources routes, processes and evaluation. Int J Hydrogen Energy 48:17383–17408. https://doi.org/10.1016/J.IJHYDENE.2023.01.175

6. Rao PC, Yoon M (2020) Potential Liquid-Organic Hydrogen Carrier (LOHC) Systems: A Review on Recent Progress. Energies 2020, Vol 13, Page 6040 13:6040. https://doi.org/10.3390/EN13226040

7. Yao QL, He M, Kong YR, Gui T, Lu ZH (2023) Y2O3-functionalized graphene-immobilized Ni–Pt nanoparticles for enhanced hydrous hydrazine and hydrazine borane dehydrogenation. Rare Met 42:3410–3419. https://doi.org/10.1007/S12598-023-02330-Z/FIGURES/6

8. Zhang X, Yao Q, Wu H, Zhou Y, Zhu M, Lu ZH (2023) Carbon-doped mesoporous TiO2-immobilized Ni nanoparticles: Oxygen defect engineering enhances hydrogen production. Appl Catal B Environ 339:123153. https://doi.org/10.1016/J.APCATB.2023.123153

9. Wan C, Li G, Wang J, Xu L, Cheng D guo, Chen F, Asakura Y, Kang Y, Yamauchi Y (2023) Modulating Electronic Metal-Support Interactions to Boost Visible-Light-Driven Hydrolysis of Ammonia Borane: Nickel-Platinum Nanoparticles Supported on Phosphorus-Doped Titania. Angew Chemie - Int Ed 62:. https://doi.org/10.1002/ANIE.202305371

10. Wan C, Liang Y, Zhou L, Huang J, Wang J, Chen F, Zhan X, Cheng D guo (2024) Integration of morphology and electronic structure modulation on cobalt phosphide nanosheets to boost photocatalytic hydrogen evolution from ammonia borane hydrolysis. Green Energy Environ 9:333–343. https://doi.org/10.1016/J.GEE.2022.06.007

11. Zhang X, Yao Q, Wang Y, Liu M, Lu ZH (2024) Hydrogen production from complete dehydrogenation of hydrazine borane on carbon-doped TiO2-supported NiCr catalysts. Inorg Chem Front 11:1683–1692. https://doi.org/10.1039/D3QI02633G

12. Song F-Z, Yang X, Xu Q, Song F-Z, Yang X, Xu Q (2020) Ultrafine Bimetallic Pt–Ni Nanoparticles Achieved by Metal–Organic Framework Templated Zirconia/Porous Carbon/Reduced Graphene Oxide: Remarkable Catalytic Activity in Dehydrogenation of Hydrous Hydrazine. Small Methods 4:1900707. https://doi.org/10.1002/SMTD.201900707

13. Wan C, Li R, Wang J, Cheng D, Chen F, Xu L, Gao M, Kang Y, Eguchi M, Yamauchi Y (2024) Silica Confinement for Stable and Magnetic Co-Cu Alloy Nanoparticles in Nitrogen-Doped Carbon for Enhanced Hydrogen Evolution. Angew Chemie Int Ed. https://doi.org/10.1002/anie.202404505

14. Cheng Y, Wu X, Xu H (2019) Catalytic decomposition of hydrous hydrazine for hydrogen production. https://doi.org/10.1039/c8se00538a

15. Sanjay KS, Zhang XB, Xu Q (2009) Room-temperature hydrogen generation from hydrous hydrazine for chemical hydrogen storage. J Am Chem Soc 131:9894–9895. https://doi.org/10.1021/JA903869Y

16. Zheng J, Zhou H, Wang CG, Ye E, Xu JW, Loh XJ, Li Z (2021) Current research progress and perspectives on liquid hydrogen rich molecules in sustainable hydrogen storage. Energy Storage Mater 35:695–722. https://doi.org/10.1016/J.ENSM.2020.12.007

17. Yoo JB, Kim HS, Kang H, Lee B, Hur NH (2014) Hollow nickel-coated silica microspheres containing rhodium nanoparticles for highly selective production of hydrogen from hydrous hydrazine. J Mater Chem A 2:18929–18937. https://doi.org/10.1039/x0xx00000x

18. Yao Q, He M, Hong X, Chen X, Feng G, Lu Z-H (2019) Hydrogen production via selective dehydrogenation of hydrazine borane and hydrous hydrazine over MoO x-promoted Rh catalyst. Int J Hydrogen Energy 44:28430–28440. https://doi.org/10.1016/j.ijhydene.2019.02.105

19. Cho SJ, Lee J, Lee YS, Kim DP (2006) Characterization of iridium catalyst for decomposition of hydrazine hydrate for hydrogen generation. Catal Letters 109:181–187. https://doi.org/10.1007/s10562-006-0081-3

20. Yao G, Chen F, Huo Z, Jin F (2016) Hydrazine as a facile and highly efficient hydrogen source for reduction of NaHCO3 into formic acid over Ni and ZnO catalysts. Int J Hydrogen Energy 41:9135–9139. https://doi.org/10.1016/J.IJHYDENE.2015.12.179

21. Bellomi S, Barlocco I, Tumiati S, Fumagalli P, Dimitratos N, Roldan A, Villa A (2023) Effect of oxygen functionalities on the hydrous hydrazine decomposition over carbonaceous materials. Dalt Trans 52:15871–15877. https://doi.org/10.1039/D3DT02310A

22. Barlocco I, Bellomi S, Tumiati S, Fumagalli P, Dimitratos N, Roldan A, Villa A (2022) Selective decomposition of hydrazine over metal free carbonaceous materials. Phys Chem Chem Phys 24:3017. https://doi.org/10.1039/d1cp05179b

23. Bellomi S, Barlocco I, Chen X, Delgado JJ, Arrigo R, Dimitratos N, Roldan A, Villa A (2023) Enhanced stability of sub-nanometric iridium decorated graphitic carbon nitride for H 2 production upon hydrous hydrazine decomposition. Phys Chem Chem Phys 25:1081. https://doi.org/10.1039/d2cp04387d

24. Zhang Z, Lu Z-H, Tan H, Chen X, Yao Q (2013) CeO x-Modified RhNi Nanoparticles Grown on rGO as Highly Efficient Catalysts for Complete Hydrogen Generation from Hydrazine Borane and Hydrazine. J Mater Chem A 3:23520–23529. https://doi.org/10.1039/x0xx00000x

25. Cheng G, Zhao P, Cao N, Luo W, Cheng G (2015) Nanoscale MIL-101 supported RhNi nanoparticles: an efficient catalyst for hydrogen generation from hydrous hydrazine. J Mater Chem A 3:12468–12475. https://doi.org/10.1039/c5ta02201k

26. Wang H, Wu L, Jia A, Li X, Shi Z, Duan M, Wang Y (2017) Ni nanoparticles

encapsulated in the channel of titanate nanotubes: Efficient noble-metal-free catalysts for selective hydrogen generation from hydrous hydrazine. Chem Eng J 332:637–646. https://doi.org/10.1016/j.cej.2017.09.126

27. Liu X, Liu Y, Wang J, Ma J (2022) Anatase-Type TiO 2-Modified Amorphous NiMo Nanoparticles with Superior Catalytic Performance toward Dehydrogenation of Hydrous Hydrazine. Ind Eng Chem Res 61:1636–1643. https://doi.org/10.1021/acs.iecr.1c03398

28. Dai H, Zhong Y, Wang P (2017) Hydrogen generation from decomposition of hydrous hydrazine over Ni-Ir/CeO2 catalyst. Prog Nat Sci Mater Int 27:121–125. https://doi.org/10.1016/J.PNSC.2016.12.012

29. Motta D, Barlocco I, Bellomi S, Villa A, Dimitratos N (2021) Hydrous hydrazine decomposition for hydrogen production using of ir/ceo2: Effect of reaction parameters on the activity. Nanomaterials 11:1340. https://doi.org/10.3390/NANO11051340/S1

30. Hafeez S, Aristodemou E, Manos G, Al-Salem SM, Constantinou A (2020) Computational fluid dynamics (CFD) and reaction modelling study of bio-oil catalytic hydrodeoxygenation in microreactors. React Chem Eng 5:1083–1092. https://doi.org/10.1039/D0RE00102C

31. Hafeez S, Aristodemou E, Manos G, Al-Salem SM, Constantinou A (2020) Modelling of packed bed and coated wall microreactors for methanol steam reforming for hydrogen production. RSC Adv 10:41680. https://doi.org/10.1039/d0ra06834a

32. Hafeez S, Al-Salem SM, Papageridis KN, Charisiou ND, Goula MA, Manos G, Constantinou A (2021) Theoretical Investigation of the Deactivation of Ni Supported Catalysts for the Catalytic Deoxygenation of Palm Oil for Green Diesel Production. Catalysts 11:747. https://doi.org/10.3390/CATAL11060747

33. Hafeez S, Barlocco I, Al-Salem SM, Villa A, Chen X, Delgado JJ, Manos G, Dimitratos N, Constantinou A (2021) Experimental and Process Modelling Investigation of the Hydrogen Generation from Formic Acid Decomposition Using a Pd/Zn Catalyst. Appl Sci 11:8462. https://doi.org/10.3390/APP11188462

34. Hafeez S, Sanchez F, Al-Salem SM, Villa A, Manos G, Dimitratos N, Constantinou A (2021) Decomposition of Additive-Free Formic Acid Using a Pd/C Catalyst in Flow: Experimental and CFD Modelling Studies. Catalysts 11:341. https://doi.org/10.3390/CATAL11030341

35. Harkou E, Hafeez S, Manos G, Constantinou A (2021) CFD Study of the Numbering up of Membrane Microreactors for CO2 Capture. Processes 9:1515. https://doi.org/10.3390/PR9091515

36. Hafeez S, Al-Salem M, Bansode A, Villa A, Dimitratos N, Manos G, Constantinou A (2022) Computational Investigation of Microreactor Configurations for Hydrogen Production from Formic Acid Decomposition Using a Pd/ C Catalyst. Ind Eng Chem Res 61:1655–1665. https://doi.org/10.1021/acs.iecr.1c04128

37. Tsiotsias AI, Charisiou ND, Harkou E, Hafeez S, Manos G, Constantinou A, Hussien AGS, Dabbawala AA, Sebastian V, Hinder SJ, Baker MA, Polychronopoulou K, Goula MA (2022) Enhancing CO 2 methanation over Ni catalysts supported on sol-gel derived Pr 2 O 3-CeO 2 : An experimental and theoretical investigation. Appl Catal B Environ 318:121836. https://doi.org/10.1016/j.apcatb.2022.121836

38. Harkou E, Hafeez S, Adamou P, Zhang Z, Tsiotsias AI, Charisiou ND, Goula MA, Al-Salem SM, Manos G, Constantinou A (2023) Different reactor configurations for enhancement of CO2 methanation. Environ Res 236:116760. https://doi.org/10.1016/j.envres.2023.116760

39. Harkou E, Adamou P, Georgiou K, Hafeez S, Al-Salem SM, Villa A, Manos G, Dimitratos N, Constantinou A (2023) Computational Studies on Microreactors for the Decomposition of Formic Acid for Hydrogen Production Using Heterogeneous Catalysts. Molecules 28:5399. https://doi.org/10.3390/MOLECULES28145399

40. Hafeez S, Harkou E, Adamou P, Barlocco I, Zanella E, Manos G, Al-Salem SM, Chen X, Delgado JJ, Dimitratos N, Villa A, Constantinou A (2023) Formic Acid Decomposition Using Palladium-Zinc Preformed Colloidal Nanoparticles Supported on Carbon Nanofibre in Batch and Continuous Flow Reactors: Experimental and Computational Fluid Dynamics Modelling Studies. Nanomaterials 13:2993. https://doi.org/10.3390/NANO13232993/S1

41. Zhang Z, Lu ZH, Tan H, Chen X, Yao Q (2015) CeOx-modified RhNi nanoparticles grown on rGO as highly efficient catalysts for complete hydrogen generation from hydrazine borane and hydrazine. J Mater Chem A 3:23520–23529. https://doi.org/10.1039/C5TA06197K

42. Dai H, Dai H Bin, Zhong YJ, Kang Q, Sun LX, Wang P (2017) Kinetics of catalytic decomposition of hydrous hydrazine over CeO2-supported bimetallic Ni–Pt nanocatalysts. Int J Hydrogen Energy 42:5684–5693. https://doi.org/10.1016/J.IJHYDENE.2016.10.160

43. Al-Thubaiti KS, Khan Z (2020) Trimetallic nanocatalysts to enhanced hydrogen production from hydrous hydrazine: The role of metal centers. Int J Hydrogen Energy 45:13960–13974. https://doi.org/10.1016/J.IJHYDENE.2020.03.093

44. Motta D, Barlocco I, Bellomi S, Villa A, Dimitratos N (2021) Hydrous hydrazine decomposition for hydrogen production using of ir/ceo2: Effect of reaction parameters on the activity. Nanomaterials 11:1340. https://doi.org/10.3390/NANO11051340/S1

45. Roselló-Merino M, Rama RJ, Díez J, Conejero S (2016) Catalytic dehydrocoupling of amine-boranes and amines into diaminoboranes: isolation of a Pt (ii), Shimoi-type, η 1-BH complex. Chem Commun 52:8389–8392

46. Luconi L, Osipova ES, Giambastiani G, Peruzzini M, Rossin A, Belkova N V, Filippov OA, Titova EM, Pavlov AA, Shubina ES (2018) Amine boranes dehydrogenation mediated by an unsymmetrical iridium pincer hydride:(PCN) vs (PCP) improved catalytic performance. Organometallics 37:3142–3153

47. Telleria A, van Leeuwen PWNM, Freixa Z (2017) Azobenzene-based ruthenium (II) catalysts for light-controlled hydrogen generation. Dalt Trans 46:3569–3578

48. Gojon C, Dureault B (1996) Spectrophotometric Study of the Reaction between Hydrazine and p.dimethylaminobenzaldehyde. J Nucl Sci Technol 33:731–735. https://doi.org/10.1080/18811248.1996.9731989

49. Berčič G, Likozar B (2022) Analysis and recompilation of kinetic data about the hydrogen production by the catalytic decomposition of hydrous hydrazine. Int J Hydrogen Energy 47:29348–29357. https://doi.org/10.1016/J.IJHYDENE.2022.06.282

50. Dai H, Dai H, Zhong Y, Kang Q, Sun L (2016) ScienceDirect Kinetics of catalytic decomposition of hydrous hydrazine over CeO 2 -supported bimetallic Ni e Pt nanocatalysts. Int J Hydrogen Energy 42:5684–5693. https://doi.org/10.1016/j.ijhydene.2016.10.160

51. Zou H, Guo F, Luo M, Yao Q, Lu Z (2020) ScienceDirect La (OH) 3 -decorated NiFe nanoparticles as efficient catalyst for hydrogen evolution from hydrous hydrazine and hydrazine borane. Int J Hydrogen Energy 45:11641–11650. https://doi.org/10.1016/j.ijhydene.2020.02.074

52. Karatas Y, Gu M, Zahmakiran M (2020) ScienceDirect Silica supported ternary NiRuPt alloy nanoparticles : Highly efficient heterogeneous catalyst for H 2 generation via selective decomposition of hydrous hydrazine in alkaline solution. 5:. https://doi.org/10.1016/j.ijhydene.2020.07.048

53. Fogler H (2016) Elements of Chemical Reaction Engineering, 5th ed.

54. Kang W, Varma A (2018) Hydrogen generation from hydrous hydrazine over Ni/CeO2 catalysts prepared by solution combustion synthesis. Appl Catal B Environ 220:409–416. https://doi.org/10.1016/J.APCATB.2017.08.053

55. Wang Y, Pan L, Chen Y, Shen G, Wang L, Zhang X, Zou JJ (2020) Mo-doped Ni-based catalyst for remarkably enhancing catalytic hydrogen evolution of hydrogen-storage materials. Int J Hydrogen Energy 45:15560–15570. https://doi.org/10.1016/J.IJHYDENE.2020.04.061

56. Lu X, Francis S, Motta D, Dimitratos N, Roldan A (2020) Mechanistic study of hydrazine decomposition on Ir(111). Phys Chem Chem Phys 22:3883–3896. https://doi.org/10.1039/C9CP06525C

57. Singh SK, Singh AK, Aranishi K, Xu Q (2011) Noble-metal-free bimetallic nanoparticle-catalyzed selective hydrogen generation from hydrous hydrazine for chemical hydrogen storage. J Am Chem Soc 133:19638–19641. https://doi.org/10.1021/JA208475Y

58. Jiang Y, Kang Q, Zhang J, Dai H-B, Wang P (2014) High-performance nickeleplatinum nanocatalyst supported on mesoporous alumina for hydrogen generation from hydrous hydrazine The catalyst shows excellent activity for selective decomposition of N 2 H 4 $H 2 O to H 2. The Ni-based catalyst may promote the. J Power Sources 273:554–560. https://doi.org/10.1016/j.jpowsour.2014.09.119

59. Jain P, Anila KA, Vinod CP (2019) Au Based Ni and Co Bimetallic Core Shell Nanocatalysts for Room Temperature Selective Decomposition of Hydrous Hydrazine to Hydrogen. ChemistrySelect 4:2734–2740. https://doi.org/10.1002/slct.201900483

60. Long J, Yao Q, Zhang X, Wu H, Lu Z-H (2022) Defects engineering of metal-organic framework immobilized Ni-La(OH) 3 nanoparticles for enhanced hydrogen production The development of low-cost, efficient, and durable catalysts to boost hydrogen production from hydrous hy-drazine (N 2 H 4 ·H 2 O) and h. Appl Catal B Environ 320:121989. https://doi.org/10.1016/j.apcatb.2022.121989

61. Lu X, Francis S, Motta D, Dimitratos N, Roldan A (2020) Mechanistic study of hydrazine decomposition on Ir(111). Phys Chem Chem Phys 22:3883–3896

62. Liu Y, Liu X, Liu X, Li Y, Ma J, Ma C (2023) TiO2 nanoparticle-supported Ni

770 catalyst for the dehydrogenation of hydrazine hydrate. Chemosphere 313:137608.
771 https://doi.org/10.1016/J.CHEMOSPHERE.2022.137608

772